Plasma Chemistry and Plasma Processing
https://doi.org/10.1007/s11090-024-10488-2

ORIGINAL PAPER

Quantitative Measurement of ROS Penetration into Model Tissue Under Plasma Treatment Using Image Processing

Bingkai Wang[1] · Nan Zhang[1] · Chengfeng Xiong[1] · Xu Yan[2] · Zilan Xiong[1]

Received: 12 March 2024 / Accepted: 10 June 2024

Abstract

Plasma dose quantification is one of the core problems in clinical of plasma medicine. The spatial-temporal distribution and the total dose of the reactive species from plasma into the processed object are especially important in clinic. In this study, we developed a measurement scheme based on image processing technology for quantifying the penetration dose of reactive oxygen species (ROS) into model tissues, and analyzed the effects of treatment conditions on the concentration distribution and the total amount. First, by establishing a numerical relationship between the color index and ROS concentration through image processing and titration experiment, the spatial concentration distribution of ROS on each sliced layer of the treated sample was calculated. Then, the ROS penetration depth was obtained through image segmentation of longitudinal sliced tissue image. Finally, by integrating the concentration of each layer and the depth, the absolute amount of ROS was obtained. Both the penetration depth and absolute amount exhibit a positive correlation with treatment time and a negative correlation with treatment distance under an Ar plasma jet treatment. A range of penetration depth of 0.5–3 mm and total dose of 0.05–0.47 μmol was obtained under the setting conditions. The effectiveness of the proposed method was confirmed by comparing with the total ROS amount measured by UV-Vis method dissolved in liquid, providing a new solution for the issue in plasma dose quantification, and is also benefit for the understanding of plasma-tissue interaction.

Keywords ROS concentration · Spatial distribution · Depth · Absolute amount · Image processing

---

✉ Xu Yan
devil-yx@163.com

✉ Zilan Xiong
zilanxiong@hust.edu.cn

[1] State Key Laboratory of Advanced Electromagnetic Technology, Huazhong University of Science and Technology, Wuhan, Hubei 430074, People's Republic of China

[2] Department of Pathophysiology, Beijing Neurosurgical Institute/ Beijing Tiantan Hospital, Capital Medical University, Beijing 100070, People's Republic of China

Introduction

Low-temperature plasma can interact with biological tissues to produce a series of medical effects. Plasma medicine research has been conducted in various fields such as skin disease treatment [1, 2], cosmetic wrinkle reduction [3], cancer therapy [4–6], and tissue ablation [7]. Similar to traditional medicine, dose is a very important issue in plasma medicine [8]. Initially, plasma treatment conditions such as voltage, flow rate, and treatment time, were used as the dose of plasma [9–11]. But these parameters are subject to many limitations, such as electrode structure, gas type, and treatment gap. The discovery of the crucial role of the reactive oxygen and nitrogen species (RONS) in clinical applications [12], makes it a natural choice to define plasma dose based on RONS. Direct gas-phase RONS concentration or indirect equivalent total oxidation potential (ETOP) are then used to define plasma dose [13, 14]. When tissues are treated by plasma, the reactive species in the gas phase does not completely works. It is the reactive species that enter the tissues that truly cause treatment effect. Therefore, it is crucial to quantitatively measure the long-lived reactive species that enter the tissues. However, the existing methods are unable to conduct accurately quantitative measurement, making dose delivery a core issue in plasma medical applications [15].

Series of studies have been conducted on this hot topic, with penetration concentration, penetration depth and spatial distribution being the key measurement parameters of focus [16–25]. For penetration concentration, it is usually converted to the measurement of the average concentration in the liquid phase, such as extracting reactive species into PBS buffer solution through grinding for liquid-phase diagnosis, or directly measuring the treated gelatin solution [17, 18, 26]. There are many studies on the measurement of penetration depth, which are mainly divided into direct methods involving the use of metallography or fluorescence microscopy to measure coloration or fluorescence depth, and indirect methods utilizing tissue covering buffer solutions of varying thickness to indirectly measure penetration depth by analyzing the components in the buffer solution [19–22]. As for spatial distribution, qualitative analysis of the distribution of reactive species is mainly conducted through the color depth in two-dimensional images [23, 24, 27]. Currently, there are nearly no effective methods for the measurement of absolute amount of RONS which penetrate into the tissues and the existing methods cannot achieve quantitative measurement of the concentration and spatial distribution of RONS in plasma-treated tissue. Meanwhile, the strong requirement of understanding the mechanisms of plasma-tissue interactions has accelerated the need for measurements of the spatial distribution and total amount of ROS. Therefore, developing new effective measurement scheme are of great importance.

The development of digital image processing technology has provided new solution for plasma diagnosis. In existing studies, a series of diagnoses of discharge states and plasma products have been achieved by combining deep learning and image processing technology [28–31]. The image contains abundant color information. In basic RGB image, various colors and intensity features can be described through the single or multiple combinations of pixel values ranging from 0 to 255 in the Red, Green, and Blue channels. Usually, the detection reagent for ROS is KI-starch, which undergoes varying degrees of blue color reaction with different concentrations of ROS. The mixing of ROS detection reagents in model tissue enables the distribution of reactive species to be detected through coloration reactions, providing possibility for quantifying ROS in model tissue using image processing method. Due to the fact that the detection reagent is mixed into the solid phase of the model tissue and the subsequent sectioning operations that may be performed, the coloration image obtained may not be a pure blue color. So the color produced by the colorimetric reaction cannot be directly described using single RGB values, and may require conversion to other color spaces to establish numerical relationship, which poses a challenge for accurate quantitative measurement of ROS.

In this study, we propose a quantitative measurement of ROS in plasma-treated model tissue based on image processing and analyzed the effects of treatment conditions on the concentration distribution and the total amount. Through titration reaction and image processing, we establish a numerical relationship between concentration and S pixels to achieve the measurement of concentration at each point on every layer of the model tissue after plasma treatment. Subsequently, image segmentation methods are employed to analyze the longitudinal section images, enabling the measurement of penetration depth. Finally, the absolute amount is obtained by integrating the size proportion relationship, and the effect of operation parameters are measured and compared.

Experimental Platform and Methods

Sample Preparation

In the plasma-treated model tissue, ROS such as O, OH, H_2O_2 and O_3 convert I^- to I_2, leading to a colorimetric reaction with starch. However, due to the short-life and high reactivity of O and OH as reactive species, their permeability to bio-macromolecules is extremely weak, and thus they are not considered as the main ROS components penetrating into tissue [16, 32, 33]. In contrast, the long-lived H_2O_2 and O_3, as the main ROS components involved in penetration, have the same reaction ratio with KI-starch, generating an equal amount of I_2 and leading to a colorimetric reaction [34, 35].

$$O_3 + 2I^- + H_2O \rightarrow I_2 + 2OH^- + O_2 \tag{1}$$

$$H_2O_2 + 2H^+ + 2I^- \rightarrow I_2 + 2H_2O \tag{2}$$

The titration reaction of sodium thiosulfate with KI-starch can yield the amount of I_2, and thus indirectly calculate the total amount of ROS, as shown in the reaction [34].

$$I_2 + 2S_2O_3^{2-} \rightarrow 2I^- + S_4O_6^{2-} \tag{3}$$

As shown in the sample preparation process in Fig. 1a, to establish the relationship between concentration and color, it is necessary to prepare standard coloration model tissues with different concentrations. A 15% gelatin (Sigma–Aldrich) is prepared as the model tissue, mixed with KI-starch (0.5% starch and 0.5% KI (Sinopharm), theoretically capable of producing a concentration of 15 mM I_2). In the proposed indirect quantification method for ROS, the colorimetric reaction is induced by the generation of I_2, which results in varying degrees of coloration at different concentrations of I_2. Therefore, H_2O_2 at different concentrations (far below the theoretical reaction concentration limitation in the model tissue) is mixed into the model tissue to generate 8 standard model tissue samples with different con-

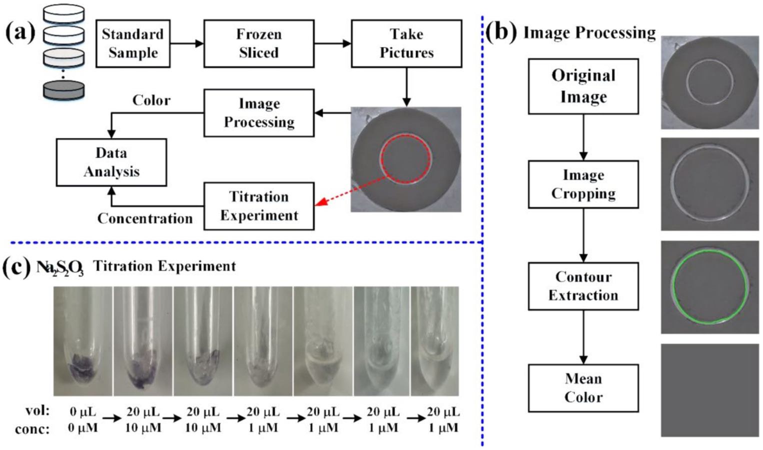

Fig. 1 (**a**) Sample preparation process, (**b**) Image processing flow, (**c**) Titration experiment operation process

centrations, each corresponding to a different coloration. Subsequently, the standard sample is placed into a freezing microtome (Leica, CM 1950) at -20 °C for 20 min before sectioning, with a section thickness of 100 µm. After circular extraction of the sections (red circular area in Fig. 1a), the color information of the circular area is obtained by capturing images of the sections with a camera for further processing. Concurrently, titration experiment is conducted on the central circular area of the sections to obtain the average ROS concentration in that region.

After obtaining the section images as shown in Fig. 1b, the image is first cropped to remove background interference. Subsequent operations involve binarization and contour extraction to obtain the contour of the central circular region in the image. Finally, the color information within this contour is computed, capturing pixel values in the RGB color space (red, green and blue), as well as the HSV color space (hue, saturation and value). The titration process was shown in Fig. 1c. Initially, 10 µM $Na_2S_2O_3$ is used to rapidly fade the section color, followed by fine titration using 1 µM solution. After each addition of 20 µL, the solution is oscillated for approximately 10 s until the color completely disappears. The volume of titrant added at each step is recorded, and combined with the actual area of the region, allowing for the calculation of ROS concentration. By executing these two processes, corresponding concentration and color information can be obtained for subsequent numerical analysis.

Data Analysis

In order to ensure the accuracy of the experiment, a total of 40 sets of data were obtained by analyzing 5 independent repeated samples for each of the 8 different concentrations of standard samples, and these data were obtained to data analysis. By comparing the results, it was found that the variation trend of the S pixel channel in the HSV color space was highly consistent with the concentration. The S pixel is a description of color depth, which is consistent with the observed phenomenon of coloration reaction depth. Multiple methods were employed for data fitting, including conventional RGB multivariate linear fitting

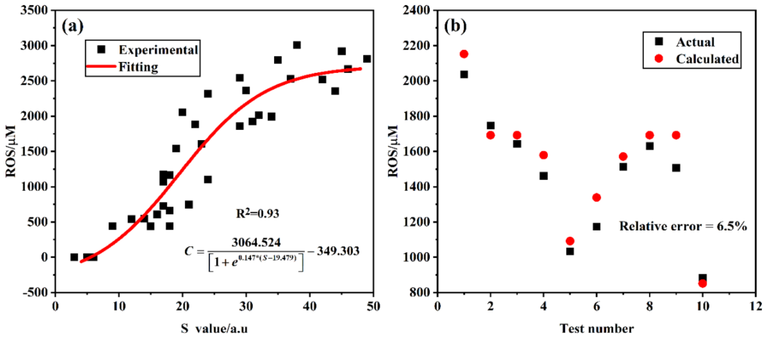

Fig. 2 (**a**) Logistic function fitting result, (**b**) Comparison of actual and calculated results

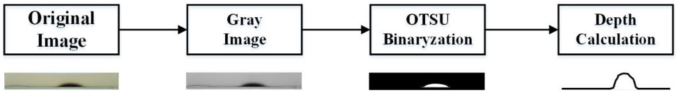

Fig. 3 Measurement process of penetration depth using longitudinal section image

(R^2=0.87), third-degree function fitting for the S pixel (R^2=0.92), and logistic function fitting for the S pixel (R^2=0.93). As shown in Fig. 2a, the logistic function with the best fitting result was selected as the model for describing the numerical relationship between color and concentration.

$$C = \frac{3064.524}{\left[1+e^{0.147*(S-19.479)}\right]} - 349.303 \tag{4}$$

Through this fitting function, the ROS concentration of each pixel on the image can be directly obtained, accurately, and without being restricted by shape.

In order to further test the accuracy of this method, the fitting result was applied to new slices to obtain the average calculated ROS concentration for each selected region of the slice. Then, titration experiments were conducted on selected region to obtain the average actual ROS concentration. As shown in Fig. 2b, the relative error values of the measurements for the 10 samples were calculated. The average relative error was within 6.5%, indicating that this method has a high measurement accuracy and can meet the requirements of practical applications.

Measurement of Penetration Depth

As shown in Fig. 3, for the measurement of penetration depth, image segmentation can be employed to extract information from longitudinal section images of the model tissue. After reading the original RGB three-channel image, it is converted into a single-channel grayscale image. Due to the high contrast between the staining region and the background, the staining region can be extracted using Otsu threshold segmentation, resulting in a binary image. Finally, by counting the number of white pixels along the radius and applying the rate relationship between pixel size at a fixed position and actual size, the actual distribution of penetration depth along the line can be obtained.

Measurement of Absolute Amount

After obtaining the ROS concentration of each pixel in each layer of sliced image, the fixed slice thickness and imaging position enable the feasible estimation of the absolute amount of penetration. The absolute amount n_p of each pixel can be calculated using Eq. (5), where C represents the concentration of each point, obtained from Eq. (4), with d representing the slice thickness (100 μm). S_p epresents the actual area of each point, which can be calculated through the proportional relationship between pixel size and actual size at a fixed position. This formula allows for the determination of the absolute amount of ROS for each point, and by summing the pixels of the sliced area *mask*, the total amount n can be obtained from Eq. (6).

$$n_p = CV_p = CS_pd \tag{5}$$

$$n = \sum\nolimits_{p\in mask} n_p \tag{6}$$

Experimental Setup and Treatment

Figure 4 shows the plasma jet experimental setup. In this study, a needle-ring structured plasma jet source is employed. The jet tube, with an inner diameter of 3 mm and outer diameter of 5 mm, is composed of quartz. Within the quartz tube, a steel needle with a diameter of 0.6 mm serves as the high-voltage electrode, connected to the pulsed power supply (Xi'an Smart Maple Electronic Technology, HVP-20P). The ground electrode consists of a 9.5 mm-wide copper foil wound around the quartz tube, positioned 5 mm above the upper edge of

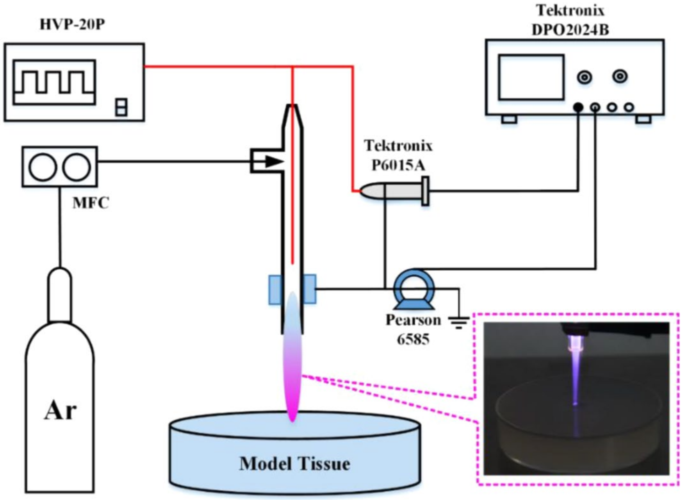

Fig. 4 Plasma jet experimental setup

the high-voltage electrode and 5 mm below the exit of the quartz tube. The parameters of the pulsed power supply are set to a voltage of 6 kV, a pulse width of 2 μs, a frequency of 8 kHz, and rise and fall time of 100 ns. The voltage and current signals are detected by a voltage probe (Tektronix P6015A) and a current monitor (Pearson 6585), respectively, and the waveforms are recorded by the oscilloscope (Tektronix DPO2024B). The emission spectrum is measured using an emission spectrometer (Ocean Optics FLAME-S). Argon gas (99.999%) is employed as the working gas with a fixed flow rate of 1 SLM.

The model tissue is placed in a Petri dish with a diameter of 60 mm, using gelatin and KI-starch identical to those in the standard sample. Under fixed voltage and flow rate, the plasma jet is applied to the model tissue surface at distances of 2 cm, 2.5 cm, and 3 cm from the bottom end of the quartz tube for treatment times of 5 min, 10 min, and 15 min, respectively. After treatment, the treated sample undergoes the standard procedures descript above, and then the concentration distribution on each layer and the penetration depth under different treatment conditions would be obtained.

To validate the results obtained by the image processing method, the UV-Vis spectrophotometer (SpectraMax M4 Multi-Mode Microplate Readers) is employed to measure the average ROS concentration (detected by starch-KI; Sinopharm) extracted from the treated sample in the liquid phase. After the treatment of blank tissue model sample with plasma jet, the superficial layer of the tissue model within a 22 mm diameter circular area was extracted. Then after the series processes such as dissolution, agitation, and centrifugation, the supernatant with the dissolved reactive species was extracted and mixed with detection reagents for UV-Vis detection to measure the average concentration in liquid phase, and the total amount of the ROS was then calculated.

Results and Discussion

V-I Characteristic and OES

The waveforms of applied voltage and current are shown in Fig. 5a with a 6 kV voltage amplitude. Two typical current pulses are observed at the rising and falling edges of the voltage pulse. The emission spectrum of the plasma jet between 200 and 800 nm is shown in Fig. 5b, clear excitation states of Ar are detected between 650 and 800 nm. As the discharge propagates from the tube to the surrounding air, due to the interaction of the plasma with the N_2, O_2, and H_2O in the environment, the excitation states of N_2 (310–450 nm), the distinct

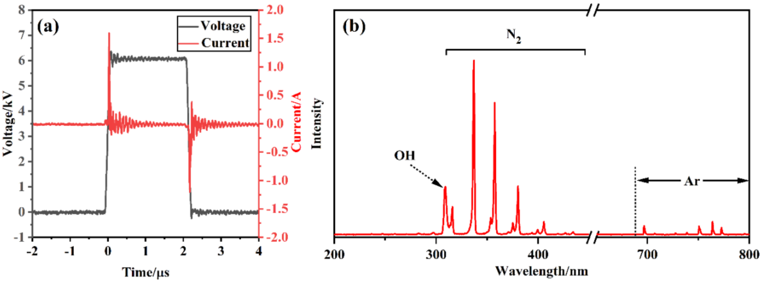

Fig. 5 (**a**) Voltage and current waveform of the plasma jet, (**b**) Optical emission spectrum

emission of OH (309 nm) is all observed. These excited state species can directly or indirectly form RONS, particularly OH, which may further participate in reactions to generate long-lived H_2O_2 and O_3.

Distribution of ROS Under Different Conditions

After treatment under various conditions and left for 30 min to fully react, visible color change reaction occurred in the model tissue, as shown in Fig. 6a. A circular blue coloration area was formed with the treatment center as the origin, and the treated point appeared darker, almost black. Similar phenomena have also been reported in existing literatures [22, 32, 36]. The diameter of the circular coloration area under various treatment conditions ranged from 6.5 mm to 20 mm, as depicted in Fig. 6b. It was observed that at the same distance, the diameter of the coloration area increased with longer treatment time. This can be attributed to the long interaction time between the plasma and the model tissue, potentially leading to a more extensive diffusion of the coloration area over a longer period. Conversely, under the same treatment time, an increase in distance resulted in a smaller diameter of the coloration area. This phenomenon is attributed to the decrease in the concentration of reactive species reaching the model tissue as the distance increases, and the reduction in the contact area between the plasma jet and the model tissue, leading to a weakening of the reaction generated by ROS and a decreasing trend in the coloration area. The two-dimensional distribution can only qualitatively characterize the effective treatment range and reaction intensity, while precise quantitative measurements of concentration and penetration depth are more important for the dose quantification in clinical application.

Quantitative Concentration Distribution of Each Sliced Layer

After treatment, the model tissues were sliced under the same freezing conditions as the standard samples. Due to the size limitation of the freezing microtome, circular area with a diameter of 22 mm (larger than the maximum diameter of the coloration area under various treatment conditions) were extracted, with the coloration area as the center. After obtaining each layer of the slice, the pixel points of the sliced area were obtained through image pro-

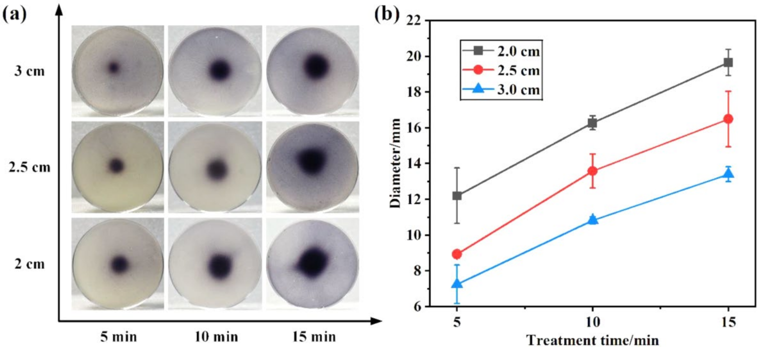

Fig. 6 (**a**) 2D coloration distribution of model tissue under various treatment conditions, (**b**) The diameter of the circular coloration area at 2, 2.5 and 3 cm for 5, 10 and 15 min

cessing, and by substituting the numerical relationship in Eq. (4), the concentration of each point could be obtained.

Taking the sliced model tissue under the condition of 2 cm and 10 min of treatment time as an example, the spatial distribution characteristics of ROS concentration were analyzed, as shown in Fig. 7. It can be observed that the ROS concentration on each layer of the slice almost consistently exhibits a distribution pattern of higher concentration at the central treatment point and lower concentration at the periphery. Furthermore, as the penetration depth increases, the average concentration of the sliced area gradually decreases. The ROS concentration at the central treatment point ranges from 1000 to 3000 μM, while the peripheral area ranges from 0 to 1000 μM, with the concentration of each layer of the slice ranging from 0 to 2500 μM. This spatial distribution pattern may be attributed to the concentrated interaction between the plasma jet and the model tissue at the point of contact, generating a stronger chemical reaction and producing more ROS. ROS diffuses from treatment point to the surrounding area. As it diffuses outward, it experiences continuous reactions, leading to a decrease in ROS concentration. This results in the characteristic of higher concentration at the center and lower concentration at the periphery. As ROS gradually penetrates into deeper layers of the model tissue, it experiences continuous reactions that result in its consumption, leading to a decrease in concentration. Therefore, the deeper the penetration, the lower the average concentration.

Penetration Depth

After processing the longitudinal section image of the treated model tissue through image segmentation, the radial distribution of penetration depth can be obtained. Taking the treated sample at 2 cm 10 min as an example, the radial distribution of penetration depth is shown in Fig. 8a. The origin of the X-axis is set at the treatment point, which also represents the position with the maximum penetration depth of 2.2 mm. As the distance from the origin increases, the penetration depth gradually decreases to 0 mm. During the plasma jet treatment process, ROS accumulate near the treatment point and continuously react as they diffuse freely towards the surrounding area. Therefore, the treatment point corresponds to the location with the maximum penetration depth, which decreases towards the periphery.

The maximum penetration depth under various treatment conditions is shown in Fig. 8b. It can be observed that the range of maximum penetration depth is approximately 1.25–3 mm. The maximum depth exhibits an increasing relationship with treatment time, and a decreasing relationship with distance. This pattern is also correlated with the accumulation of ROS: as the treatment time increases, the accumulation of ROS also increases,

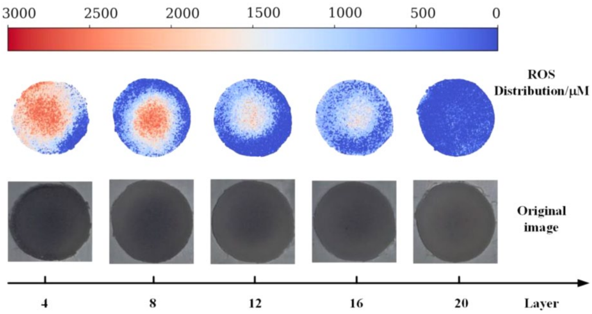

Fig. 7 ROS distribution of layer 4, 8, 12, 16 and 20 at 2 cm, 10 min

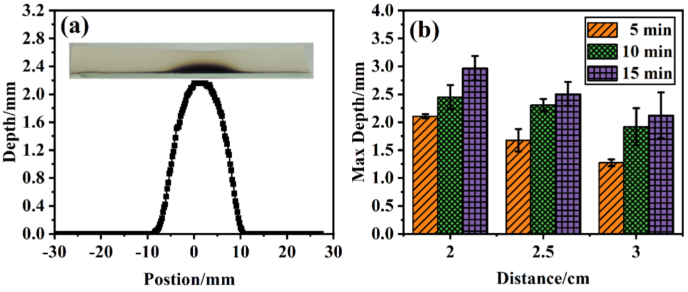

Fig. 8 (**a**)Penetration depth distribution in the longitudinal section at 2 cm 10 min, (**b**) The max penetration depth at 2, 2.5 and 3 cm for 5, 10 and 15 min

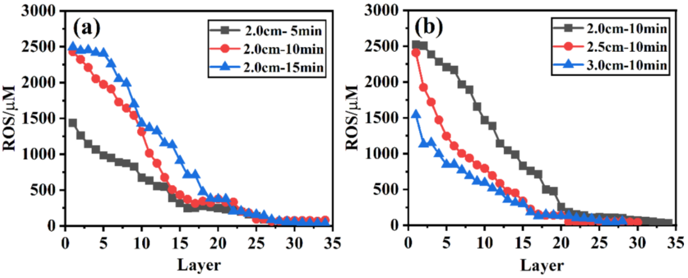

Fig. 9 (**a**) Average concentration with layer number at 2 cm 5 min,10 min,15 min, (**b**) Average concentration with layer number at 10 min 2 cm, 2.5 cm, 3 cm

leading to enhanced penetration capability. With an increase in distance, the accumulation of ROS in the treatment area decreases, resulting in reduced penetration depth. In the existing literature, the maximum penetration depth of H_2O_2 into muscle tissue obtained by treating with He + O_2 plasma jet was reported to be approximately 0.5–1.5 mm [26]. And another treatment of model tissue with He plasma jet resulted in a maximum H_2O_2 penetration depth of approximately 1.5 mm [22]. The range of 1.25–3 mm measured in our study falls within the same order of magnitude. Considering the variations in plasma sources and treatment conditions, such differences are deemed acceptable.

Absolute Amount

Figure 9a and b show the variation of average ROS concentration with the layer number under different treatment time and distance. At the same distance of 2 cm but different treatment times, the range of average concentration variation is 0-2500 μM, with the concentration gradually decreasing as layer number increases. In general, with longer treatment time, the average concentration at the same layer number is higher. This is because the longer interaction time between the plasma and the model tissue results in a greater accumulation of ROS. Under the same conditions, the corresponding ROS concentration at the same layer number is higher. Under the same treatment time of 10 min but different distances, the range of average concentration variation is also 0-2500 μM, with the concentration gradually decreasing as the layer number increases. This is due to the weaker interaction between the

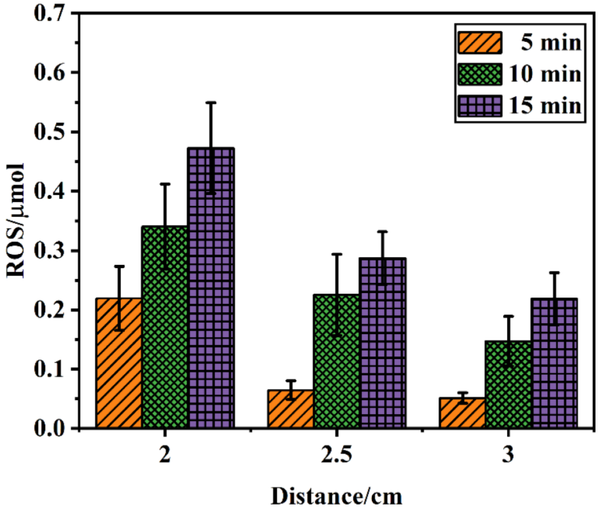

Fig. 10 ROS absolute amount at 2, 2.5 and 3 cm for 5, 10 and 15 min

plasma and the model tissue as the distance increases, resulting in a smaller accumulation at the same time and a lower ROS concentration at the corresponding layer number. In existing reports, the average H_2O_2 concentration permeating into the tissue obtained by treating mouse skin with He+O_2 plasma jet was approximately 2700 μM [17], while the average concentration obtained by treating a 2% gelatin solution with KINPen was approximately 2500 μM [18]. The range of 0-2500 μM measured in our study is within the same order of magnitude. Considering the differences in plasma sources and treatment conditions, such differences are deemed acceptable.

After obtaining the ROS concentration for each point in every slice, the absolute amount of ROS for each point and each slice can be obtained by substituting into Eqs. 1 and 2. The accumulation of each slice can then yield the total absolute amount of ROS in the model tissue. The absolute amount of ROS under various treatment conditions is illustrated in Fig. 10, with a range of variation between 0.05 and 0.47 μmol. The absolute amount of ROS exhibits a monotonically increasing relationship with treatment time and a monotonically decreasing relationship with distance. The absolute amount of ROS is directly related to the accumulation of ROS in the treatment area during the processing. During the plasma jet treatment of the model tissue, ROS accumulates in the treatment area and permeates into the model tissue. As the treatment time increases, the accumulation of ROS also increases, resulting in a greater total absolute amount in the tissue model. Conversely, with an increase in distance, the accumulation of ROS in the treatment area decreases, leading to a reduction in the absolute amount of ROS.

Comparison with the UV-Vis Method

To further validate the results obtained by the image processing, a comparative analysis of total ROS amount was conducted with UV-Vis method as descript in Sect. 2.5. The comparison result is shown in Fig. 11. It can be seen from the results in the test samples, the total ROS amount obtained by the image processing method in tissue model and by the UV-Vis method dissolved in liquid are numerically close. These are in the same order of magnitude

Fig. 11 The comparison of the total ROS amount obtained by the image processing method and the UV-Vis method

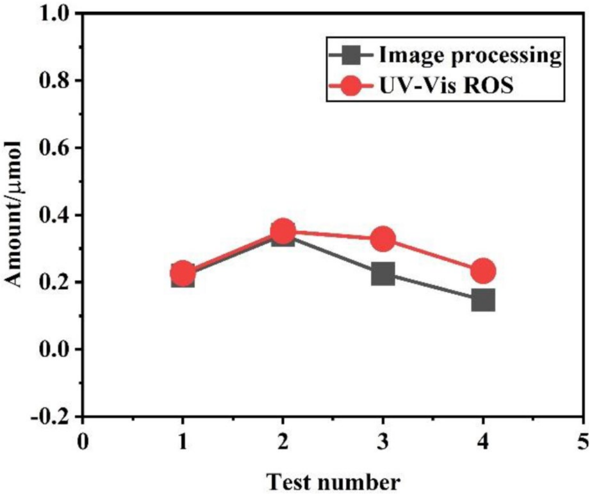

as existing reported results, positively demonstrating the effectiveness of the image processing method.

Conclusion

In response to the dose issue in plasma medical applications, this study proposed a measurement scheme based on digital image processing to quantify the penetration dose of ROS into model tissue and analyzed the effects of treatment distance and time on the penetration depth and total amount of ROS into the model tissue. A characteristic of high concentration in the center and low concentration at the periphery was found in the treated sample. As the penetration depth increases, the average concentration on each sliced layer gradually decreases within a range of 0-2500 μM. The ROS penetration depth exhibits the characteristics of deepest penetration at the treatment point, and gradually decreases around the center of the point. Additionally, the maximum penetration depth demonstrates a monotonically increasing correlation with treatment time and a monotonically decreasing correlation with distance. The maximum absolute penetration amount of ROS was achieved under the treatment condition of 2 cm distance and 15 min, with a value of approximately 0.47 μmol. Similarly, the absolute amount is positively correlated with treatment time and negatively correlated with distance. Both the variation in penetration depth and absolute amount with distance and treatment time are related to the cumulative effects of ROS in the region around the plasma jet treatment point. The proposed method provides accurately measurements for the spatial distribution and absolute amount of ROS that penetrate into model tissues under plasma treatment, and also a robust reference for the dose quantification in medical applications.

Author Contributions Author Contributions Bingkai Wang: Writing – Original draft, Visualization, Validation, Software, Methodology, Formal analysis. Nan Zhang: Validation, Investigation, Data curation. Chengfeng Xiong: Validation, Investigation, Data curation. Zilan Xiong: Writing review & editing, Supervision,

Resources, Project administration, Methodology. Xu Yan: Writing review & editing, Supervision, Project administration.

Funding This work was supported in part by the National Natural Science Foundation of China under Grant 51907076, 52177145 and 52077006, and in part by the Beijing Natural Science Foundation under Grant 7232332.

Data Availability Data is provided within the manuscript or supplementary information files.

Declarations

Competing Interests The authors declare no competing interests.

References

1. Xiong Z, Roe J, Grammer TC, Graves DB (2016) Plasma treatment of Onychomycosis. Plasma Process Polym 13:588–597
2. Xiong Z, Huang R, Zhu Y et al (2021) On the mechanisms of surface microdischarge plasma treatment of onychomycosis: penetration, uptake, and chemical reactions. Plasma Process Polym 18:1–7
3. Scarano A, Carinci F, Festa F et al (2020) Periauricular wrinkles removed with voltaic arc dermabrasion (Atmospheric plasma technique). J Cosmet Dermatol 19:1709–1714
4. Faramarzi F, Zafari P, Alimohammadi M et al (2021) Cold Physical plasma in Cancer Therapy: mechanisms, signaling, and immunity. Oxid Med Cell Longev 2021:1–19
5. Miebach L, Freund E, Clemen R et al (2022) Conductivity augments ROS and RNS delivery and tumor toxicity of an argon plasma jet. Free Radic Biol Med 180:210–219
6. Chaturvedi Misra V, Pai BG, Tiwari N et al (2023) Excitation frequency effect on breast Cancer Cell Death by Atmospheric pressure Cold plasma. Plasma Chem Plasma Process 43:467–490
7. Bekeschus S, Moritz J, Helfrich I et al (2020) Ex vivo exposure of human melanoma tissue to cold physical plasma elicits apoptosis and modulates inflammation. Appl Sci 10:1–8
8. Dai X, Zhang Z, Zhang J, Ostrikov K (2020) Dosing: the key to precision plasma oncology. Plasma Process Polym 17:1–15
9. Lin A, Gromov M, Nikiforov A et al (2023) Characterization of non-thermal dielectric barrier discharges for plasma medicine: from Plastic Well plates to skin surfaces. Plasma Chem Plasma Process 43:1587–1612
10. Chen C, Liu D, Yang A et al (2018) Aqueous reactive Oxygen species Induced by he+O2 plasmas: Chemistry pathways and Dosage Control approaches. Plasma Chem Plasma Process 38:89–105
11. Oh J-S, Szili EJ, Gaur N et al (2016) How to assess the plasma delivery of RONS into tissue fluid and tissue. J Phys D Appl Phys 49:304005
12. Graves DB (2012) The emerging role of reactive oxygen and nitrogen species in redox biology and some implications for plasma applications to medicine and biology. J Phys D Appl Phys 45:263001
13. Cheng H, Xu J, Li X et al (2020) On the dose of plasma medicine: equivalent total oxidation potential (ETOP). Phys Plasmas 27:063514
14. Shekhter AB, Pekshev AV, Vagapov AB et al (2020) Dose-dependent effect of plasma-chemical NO-containing gas flow on wound healing. An experimental study. Clin Plasma Med 19–20:100101
15. Szili EJ, Hong SH, Oh JS et al (2018) Tracking the penetration of plasma reactive species in tissue models. Trends Biotechnol 36:594–602
16. Nie L, Yang Y, Duan J et al (2018) Effect of tissue thickness and liquid composition on the penetration of long-lifetime reactive oxygen and nitrogen species (RONS) generated by a plasma jet. J Phys D Appl Phys 51:345204
17. Duan J, Gan L, Nie L et al (2019) On the penetration of reactive oxygen and nitrogen species generated by a plasma jet into and through mice skin with/without stratum corneum. Phys Plasmas 26:043504
18. Labay C, Roldán M, Tampieri F et al (2020) Enhanced generation of reactive species by Cold plasma in gelatin solutions for selective Cancer cell death. ACS Appl Mater Interfaces 12:47256–47269
19. Thulliez M, Bastin O, Nonclercq A et al (2021) Gel models to assess distribution and diffusion of reactive species from cold atmospheric plasma: an overview for plasma medicine applications. J Phys D Appl Phys 54:463001

20. XU Z, LAN Y, MA J et al (2020) Applications of atmospheric pressure plasma in microbial inactivation and cancer therapy: a brief review. Plasma Sci Technol 22:103001
21. Duan J, Lu X, He G (2017) On the penetration depth of reactive oxygen and nitrogen species generated by a plasma jet through real biological tissue. Phys Plasmas 24:073506
22. Szili EJ, Bradley JW, Short RD (2014) A 'tissue model' to study the plasma delivery of reactive oxygen species. J Phys D Appl Phys 47:152002
23. Kawasaki T, Sato A, Kusumegi S et al (2016) Two-dimensional concentration distribution of reactive oxygen species transported through a tissue phantom by atmospheric-pressure plasma-jet irradiation. Appl Phys Express 9:076202
24. Kawasaki T, Kuroeda G, Sei R et al (2018) Transportation of reactive oxygen species in a tissue phantom after plasma irradiation. Jpn J Appl Phys 57:01AG01
25. Liu D, He T, Liu Z et al (2018) Spatial-temporal distributions of ROS in model tissues treated by a he+O 2 plasma jet. Plasma Process Polym 15:1800057
26. Nie L, Yang Y, Duan J et al (2018) Effect of tissue thickness and liquid composition on the penetration of long-lifetime reactive oxygen and nitrogen species (RONS) generated by a plasma jet. J Phys D Appl Phys 51
27. Liu D, He T, Liu Z et al (2018) Spatial-temporal distributions of ROS in model tissues treated by a he+O2 plasma jet. Plasma Process Polym 15:1–8
28. Zou Z, Han R, Lu C, Xiong Z (2021) Detection of long-lived species in plasma-activated water, based on digital colorimetry. Plasma Process Polym 18:1–12
29. Lu C, Xiong Z (2022) Operation mode recognition of surface microdischarge based on the gray level histogram. Plasma Process Polym 19:1–10
30. Yuan Z, Ye Q, Wang Y, Guo Z (2021) State Recognition of Surface discharges by visible images and machine learning. IEEE Trans Instrum Meas 70:1–11
31. Wang Y, Ye Q, Guo Z (2021) Surface discharge status diagnosis based on optical image chromaticity coordinates. IEEE Trans Plasma Sci 49:1574–1579
32. Suresh M, Kondeti VSSK, Bruggeman PJ (2022) Production and diffusion of H 2 O 2 during the interaction of a direct current pulsed atmospheric pressure plasma jet on a hydrogel. J Phys D Appl Phys 55:185201
33. He T, He Y, Wang Y et al (2022) Visualization of the surface distributions of reactive oxygen species on model human tissues treated by a he+O2 plasma jet. Eur Phys J D 76:1–7
34. Sattsangi PD (2011) A microscale approach to chemical kinetics in the general chemistry laboratory: the potassium iodide hydrogen peroxide iodine-clock reaction. J Chem Educ 88:184–188
35. Al-Baarri AN, Legowo AM, Abduh SBM et al (2019) Production of ozone and the simple detection using potassium iodide titration method. IOP Conf Ser Earth Environ Sci 292:012062
36. Omran A, Busco G, Dozias S et al (2019) Distribution and penetration of reactive oxygen and nitrogen species through a tissue phantom after plasma Gun treatment. 24th Int Symp Plasma Chem 1–5